Earth and Planetary Science Letters 594 (2022) 117737

Contents lists available at ScienceDirect

Earth and Planetary Science Letters

www.elsevier.com/locate/epsl

A multiple sulfur record of super-large volcanic eruptions in Archaean pyrite nodules

Andrea Agangi [a,b,*], Axel Hofmann [b], Benjamin Eickmann [c,d], Frantz Ossa Ossa [b,e], Perinne Tyler [f], Boswell Wing [g], Andrey Bekker [h,b]

[a] Department of Earth Resource Science, Akita University, Akita, Japan
[b] Department of Geology, University of Johannesburg, South Africa
[c] Departamento de Geociencias, Universidad de los Andes, Bogotá, Colombia
[d] Department of Geosciences, University of Tübingen, Tübingen, Germany
[e] School of Earth & Environmental Sciences, Cardiff University, Cardiff CF10 3AT, UK
[f] Research School of Earth Sciences, the Australian National University, Canberra, Australia
[g] Department of Geological Sciences, University of Colorado, Boulder, USA
[h] Department of Earth and Planetary Sciences, University of California, Riverside, CA 92521, USA

ARTICLE INFO

Article history:
Received 25 February 2022
Received in revised form 29 May 2022
Accepted 13 July 2022
Available online xxxx
Editor: F. Moynier

Keywords:
Archaean
multiple-S isotopes
Kaapvaal
pyrite

ABSTRACT

Archaean supracrustal rocks carry a record of mass-independently fractionated S that is interpreted to be derived from UV-induced photochemical reactions in an oxygen-deficient atmosphere. Experiments with photochemical reactions of SO_2 gas have provided some insight into these processes. However, reconciling experimental results with the multiple S isotopic composition of the Archaean sedimentary record has proven difficult and represents one of the outstanding issues in understanding the Archaean surface S-cycle. We present quadruple S isotope data (^{32}S, ^{33}S, ^{34}S, ^{36}S) for pyrite from Mesoarchaean carbonaceous sediments of the Dominion Group, South Africa, deposited in an acidic volcanic lake, which help reconcile observations from the Archaean sedimentary record with the results of photochemical experiments. The data, which show low $\Delta^{33}S/\delta^{34}S$ ratios (mostly $\ll 1$) and very negative $\Delta^{36}S/\Delta^{33}S$ ratios (-4 and lower), contrast with the composition of most Archaean sedimentary sulfides and sulfates, having $\Delta^{36}S/\Delta^{33}S \sim -1$ (the so-called 'Archaean reference array'), but match those of modern photochemical sulfate aerosols produced in the stratosphere, following super-large volcanic eruptions, and preserved in Antarctic ice. These data are also consistent with the results of UV-irradiation experiments of SO_2 gas at variable gas pressure. The S isotope composition of the Dominion Group pyrite is here interpreted to reflect the products of photolysis in a low-oxygen-level atmosphere at high SO_2 pressure during large volcanic eruptions, mixed with Archaean 'background' (having a composition broadly similar to the Archaean reference array) S pools. It is inferred that high sedimentation rates in a terrestrial basin resulted in an instantaneously trapped input of atmospheric S during short-lasted depositional intervals, which faithfully represents transient photochemical signals in comparison with marine sedimentary records.

1. Introduction

The Archaean atmosphere was dramatically different from the modern one not only in being oxygen-deficient, but also in having much higher CO_2, CH_4 and H_2 levels, half or less atmospheric pressure, and generally moderate temperature (Catling and Zahnle, 2020). Under oxygen-deficient conditions and with oxidative continental weathering largely lacking, the Archaean geochemical cycle of S was very different from that of today. The Archaean oceans were sulfate-poor and atmospherically sourced S dominated their S budget (Canfield et al., 2000; Crowe et al., 2014; Ueno, 2014). As a consequence of low sulfate concentrations, Archaean marine sediments typically record a narrow range of $\delta^{34}S$ values (approximately -5–$+5$ ‰; Bekker et al., 2009; Canfield, 2005; Habicht et al., 2002). In addition, the Archaean sedimentary record is characterised by anomalous S isotope composition of sulfide and sulfate minerals with mass-independent fractionation of sulfur isotopes (MIF-S), a phenomenon derived from the interaction of UV solar

* Corresponding author.
E-mail address: andrea.agangi@gmail.com (A. Agangi).

https://doi.org/10.1016/j.epsl.2022.117737

radiation with SO_2 gas in an oxygen-poor atmosphere (Farquhar et al., 2001; Pavlov and Kasting, 2002).

Laboratory experiments have revealed that irradiation of gaseous S species (mostly SO_2) with UV light induces photochemical reactions that result in the production of oxidised species (SO_3, SO_4^{2-}) with negative $\Delta^{33}S$ values and elemental S with positive $\Delta^{33}S$ values (Farquhar et al., 2001). The specific S-isotope fractionation trends in these reactions are strongly dependent on the wavelength of the incident light and the gas composition and pressure used during the experiments (Endo et al., 2016; Farquhar et al., 2001; Whitehill et al., 2015). Thus, specific, broad $\Delta^{33}S$–$\delta^{34}S$ and $\Delta^{36}S$–$\Delta^{33}S$ relationships observed in the sedimentary rock record spanning from the Eoarchaean to the Neoarchaean, called Archaean reference arrays (ARA), are thought to be a fingerprint of the photochemical pathways of isotopic fractionation and to broadly reflect contemporaneous atmospheric composition (Halevy, 2013; Farquhar et al., 2001, 2007; Masterson et al., 2011; Ono et al., 2013; Zerkle et al., 2012). For example, deviations from the ARA in the Neoarchaean sedimentary records on the Kaapvaal craton have been linked to high atmospheric CH_4 levels and CH_4/CO_2 ratios (Zerkle et al., 2012). The Mesoarchaean S record, in contrast, is characterised by limited $\Delta^{33}S$ range in comparison to both the Palaeo- and Neoarchaean records, a feature that has been ascribed either to partial shutdown of mass-independent S isotope fractionation processes due to a transient atmospheric oxygenation (Ohmoto et al., 2006) or to a different atmospheric composition (Farquhar et al., 2007).

Importantly, photochemical experiments so far have not succeeded in reproducing the ARA and yielded much lower $\Delta^{33}S/\delta^{34}S$ and $\Delta^{36}S/\Delta^{33}S$ ratios (<1 and <-1, respectively). Instead, the experimental results appear to match well the MIF-S trends observed in modern volcanic sulfates preserved in Antarctic ice, which are interpreted to have been influenced by photolysis and photoexcitation reactions during large stratospheric volcanic eruptions (Baroni et al., 2007, 2008; Savarino et al., 2003). This mismatch has not been fully resolved so far, and represents one of the outstanding issues in the understanding of the S-cycle on the Archaean Earth.

In this study, we use quadruple S isotope ratios of sedimentary to diagenetic pyrite to characterise S fluxes to intracontinental lakes in a volcanically active Mesoarchaean environment. While the present understanding of the Archaean S cycle is largely based on marine sedimentary rocks, only a few studies so far have explored the S cycle in Archaean terrestrial settings (Guy et al., 2012, 2014; Maynard et al., 2013), reflecting the scarce preservation of non-marine sediments during that time. Our results suggest a link between the Archaean sedimentary record and the modern S isotope signal of super-large volcanic eruptions, as well as photochemical experiments under controlled conditions. The S-isotope data indicate mixing of mantle-derived S that has undergone photochemical processing in the predominantly anoxic Archaean atmosphere under 'background' conditions with S delivered to the atmosphere during large volcanic eruptions via a SO_2-rich volcanic plume.

2. Geological setting – the Dominion Group

The Dominion Group of the Kaapvaal craton, South Africa, is the oldest preserved intracratonic volcanic succession (Fig. 1). It was deposited in a failed rift and rests on an extensive nonconformity that represents craton-scale emergence and erosion (Grandstaff et al., 1986; Jackson, 1992). The up to 2700 m-thick succession is dominated by massive, amygdaloidal mafic to intermediate volcanic rocks, felsic porphyry and strongly rheomorphic ignimbrites interpreted to have been deposited largely in a subaerial environment (Agangi et al., 2020; Jackson, 1992). The Dominion Group

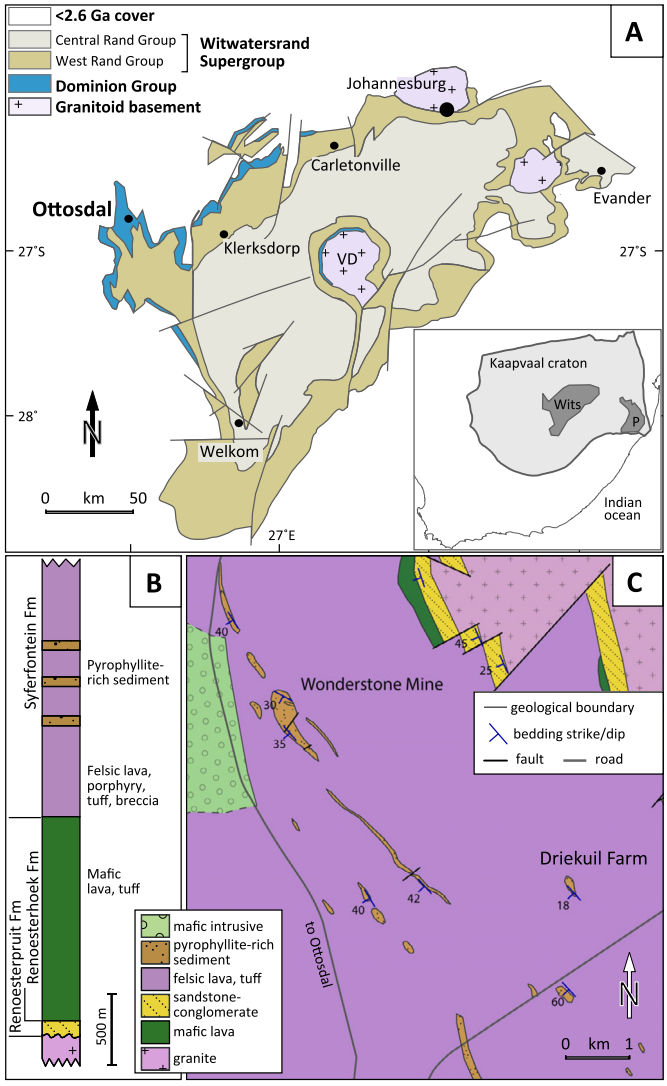

Fig. 1. Simplified geology of the Dominion Group and surrounding areas. **A** Geological map of the Witwatersrand basin (Dominion Group shown in blue) and location in the Kaapvaal craton (inset). Wits – Witwatersrand Supergroup, P – Pongola Supergroup, VD – Vredefort Dome. **B** Stratigraphic section of the Dominion Group in the area surrounding the town of Ottosdal (modified from Jackson, 1992). **C** Geological map of the area north of Ottosdal (modified from Nel et al., 1937; Von Backström, 1962). (For interpretation of the colours in the figure(s), the reader is referred to the web version of this article.)

is composed of three formations: the sedimentary Rhenosterspruit Formation, the mostly mafic volcanic Rhenosterhoek Formation and the mostly volcanic, felsic-dominated Syferfontein Formation. The presence of pyroclastic deposits (ignimbrites) intercalated with Syferfontein Formation lavas indicates explosive volcanism with Plinian eruption style typical of subaerial intracontinental volcanic provinces. Recent U–Pb zircon ages of felsic volcanic rocks suggest an age of ca. 2960 Ma (Paprika et al., 2021; cf. Armstrong et al., 1991). Ages of the basement granite as young as ca. 3031 Ma (Robb and Meyer, 1995) provide the maximum age for the cycle of granite intrusion, uplift, erosion and deposition of volcanic rocks. The studied samples are from carbonaceous sediments intercalated with felsic volcanic rocks of the Syferfontein Formation that form the upper part of the Dominion Group sequence (Fig. 1B, C). These sediments are inferred to have been deposited rapidly in large volcanic lakes that formed as a direct result and following large-scale volcanic eruptions (Agangi et al., 2021).

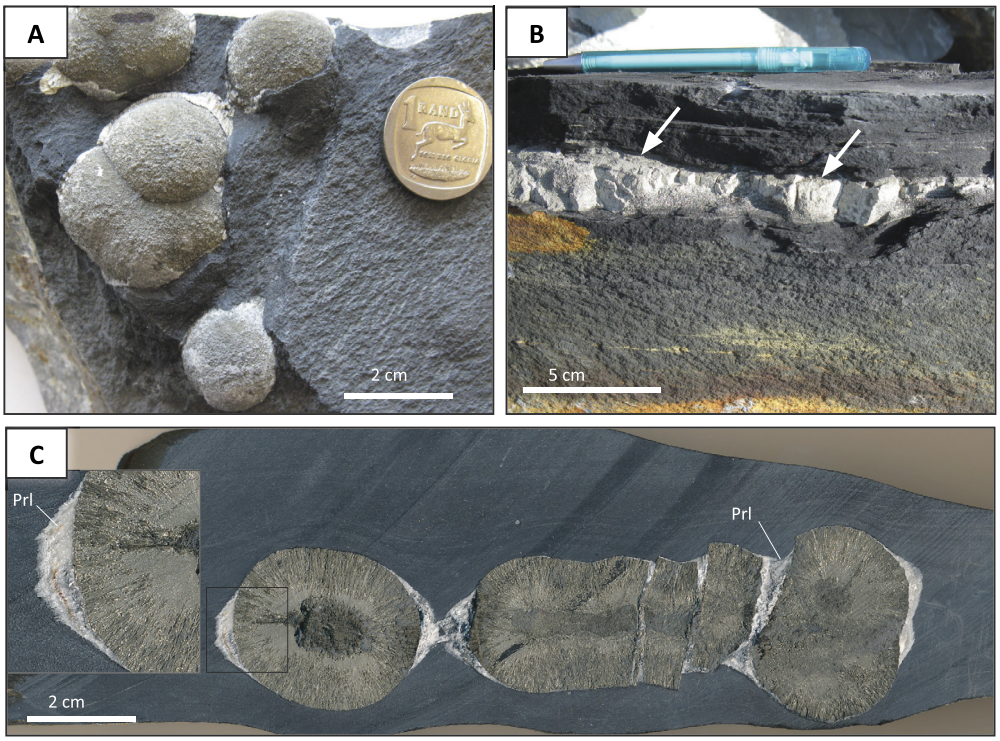

Fig. 2. Field and hand specimen textures of diagenetic pyrite nodules and layers in the Dominion Group. **A** Nodules preserved in carbonaceous shale. **B** Bedding-parallel pyrite layer (indicated by arrows) in carbonaceous shale. **C** Slab of carbonaceous shale sectioned perpendicular to bedding and containing pyrite nodules with inclusion-rich cores and radially textured rims. Note sedimentary laminae wrapped around the nodules, suggesting their pre-compaction origin. Pyrophyllite growing in pressure shadows and cracks (Prl, identified with Raman peaks at 264 and 710 cm^{-1}) shows evidence of growth at several stages during sediment compaction (see inset). All samples are from Wonderstone Mine.

3. Results

3.1. Pyrite textures and host-rocks

In the study area around the town of Ottosdal, sediments dipping at an average angle of 35° to the southwest are intercalated with felsic volcanic rocks and crop out discontinuously for a minimum of several km along strike (Fig. 1). The sediments are colloquially known as Wonderstone and are quarried for their unique characteristics of heat resistance. Sedimentary packages are typically <100 m thick and consist of carbonaceous shale and turbiditic, lithic arenite metamorphosed at lower greenschist facies conditions. The presence of pyrophyllite and diaspore, and the absence of andalusite, constrain the maximum temperature of metamorphism to ca. 320 °C (Agangi et al., 2021). The mineral composition is dominated by pyrophyllite and variable amounts of K-mica, with accessory diaspore, rare earth element (REE)-Al-phosphate and rutile. The shale contains up to 1.5 wt% total organic carbon with $\delta^{13}C$ values down to −46.6 ‰ (Agangi et al., 2021).

The carbonaceous sedimentary rocks contain sedimentary to early diagenetic pyrite occurring as nodules, semi-massive layers and disseminated fine-grained crystals (Fig. 2A and B). The nodules are preferentially developed in discrete sulfidic horizons of black (carbon-rich) shale and were observed at Wonderstone Mine and in a quarry on Driekuil Farm (Fig. 1). The nodules have subspherical to ellipsoidal shapes and occur isolated or in clusters of two or more coalescing forms with diameters of up to 8 cm. In cross-section, they often show concentric textures where a core and a rim can be identified (Fig. 2C). The nodules are wrapped by the laminae of the hosting shale, implying formation at an early diagenetic, pre-compaction stage. Compaction led to formation of pressure shadows and cracks in some nodules that are filled with pyrophyllite (Fig. 2C).

Under the optical microscope, the rims of pyrite nodules are composed of radially oriented bladed pyrite with spearhead twins (Fig. 3A and B). The cores comprise irregular domains with variable density of inclusions (Fig. 3A and C). The inclusion-rich portions of the cores are composed of fine-grained (<10 µm), euhedral pyrite set in a carbonaceous, phyllosilicate-rich matrix or cemented with pyrite. Several nodules also have relatively massive domains displaying inclusions of 1 µm or less in size (Fig. 3C).

Other nodules do not show radial arrangement of crystals and are composed of micrometre-scale euhedral, locally inclusion-rich pyrite (Fig. 3D), similar to the disseminated pyrite found in the rock matrix and in semi-massive pyrite layers. In some of these nodules, euhedral pyrite is cemented with inclusion-rich pyrite (Fig. 3D inset). Semi-massive pyrite layers are formed by fine-grained euhedral crystals, up to 100–200 µm in size, finely intergrown with matrix minerals (Fig. 3E).

Pyrite also occurs in altered porphyritic volcanic rocks intercalated with sediments at Wonderstone Mine, as disseminated euhedral grains and veinlets associated with pyrophyllite and quartz (Fig. 3F). Based on optical microscopy, Raman spectroscopy and SEM, the pyrite nodules contain inclusions of pyrophyllite, carbonaceous matter and chalcopyrite (Supplementary Fig. 1). Chalcopyrite was also observed in relatively massive pyrite, forming veinlets cross-cutting the nodules and in volcanic rocks.

3.2. Quadruple S isotope analyses

Quadruple S isotope analyses were conducted on microdrilled powders using gas-source mass-spectrometry and sulfur fluorination method combined with in situ ion probe (SHRIMP-SI) analyses on all main textural types of pyrite (see Analytical Methods in Supplementary Information). The results are presented in Supplementary Table 1, Fig. 4, 5 and Supplementary Fig. 2. The data show

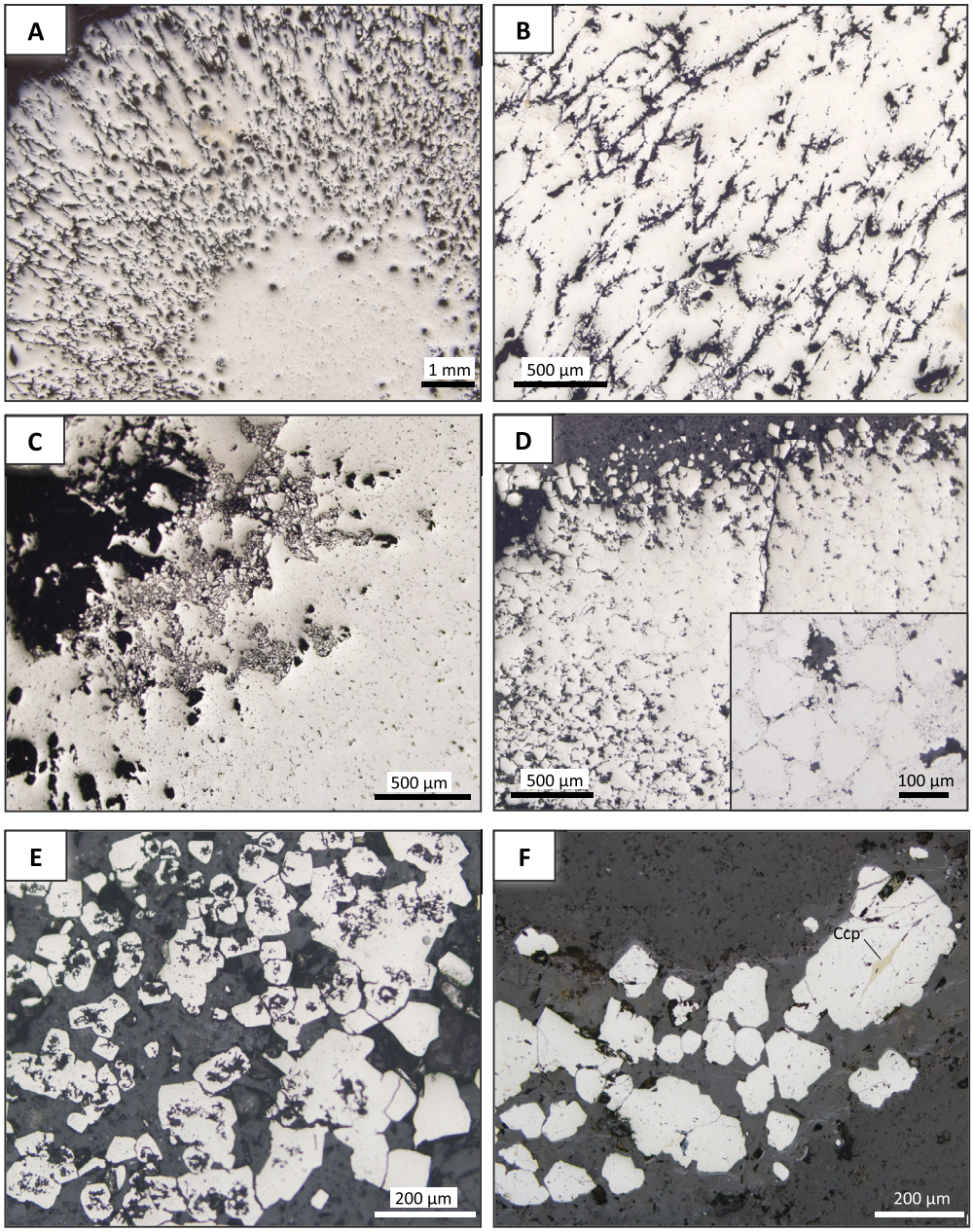

Fig. 3. Microtextures of diagenetic pyrite nodules and layers in the Dominion Group. **A** Concentric nodule with radially textured rim. Sample DWS35. **B** Close-up image of radial textures in A. **C** The core of a concentric nodule has a composite texture, with inclusion-rich (left of image) and relatively massive (right) portions. Sample DWS49A. **D** (and inset) Non-concentric nodule composed of euhedral pyrite cemented by fine-grained pyrite. Sample DWS48. **E** Fine-grained euhedral-subhedral pyrite forming semi-massive layers. The inclusions at the centre of pyrite are composed of the same mineral as the matrix. Sample DWS64. **F** Subhedral pyrite in a quartz-pyrophyllite vein cross-cutting a porphyritic volcanic rock (Ccp chalcopyrite). Sample DWS55B. All images are in plane-polarised reflected light.

great complexity and sulfur isotope values are largely dependent on texture.

Sulfur isotope analyses of microdrilled pyrite nodules

Values of $\delta^{34}S$ for two pyrite nodules with radial fabric range between +2.0 and +6.5 ‰, and $\Delta^{33}S$ values range between +0.2 and +0.7 ‰ V-CDT, with one outlier at $\delta^{34}S = -3.2$ ‰ and $\Delta^{33}S = 0.0$ ‰ (Fig. 4A). When the results are plotted according to the relative distance from the centre, clear patterns in both $\delta^{34}S$ and $\Delta^{33}S$ values are observed in both nodules (Fig. 5). Both $\delta^{34}S$ and $\Delta^{33}S$ values decrease from core to rim, with the exception of one outlier of inclusion-rich pyrite. In contrast, $\Delta^{36}S$ values, ranging from −5.9 to −4.0 ‰, increase from core to rim. In the $\Delta^{33}S$ versus $\delta^{34}S$ plot (Fig. 4A), the data are tightly grouped, excluding one outlier, and plot along a line with a shallow positive slope of 0.11. This slope contrasts with the ARA having the slope of 0.9, but it closely fits the results of photolysis experiments of SO_2 gas using 190–220 nm wavelength Xe laser source (Ono et al., 2013; Whitehill and Ono, 2012).

In $\Delta^{36}S$ versus $\Delta^{33}S$ plots (Fig. 4B), the data for microdrilled powders plot in the second quadrant with a strongly negative $\Delta^{36}S/\Delta^{33}S$ ratio, approximately −9 or even lower. When examined in more detail, the data appear to plot along two distinct trends. One trend, represented by analyses of inclusion-rich core domains, passes through the origin and has a slope of approximately −9. The second trend, represented by massive core domains and radial rims, intersects the y axis at $\Delta^{36}S = -3.5$ ‰ and has a slope of approximately −4. Both trends are clearly different from the ARA of linear data trends found for Archaean sedimentary rocks that

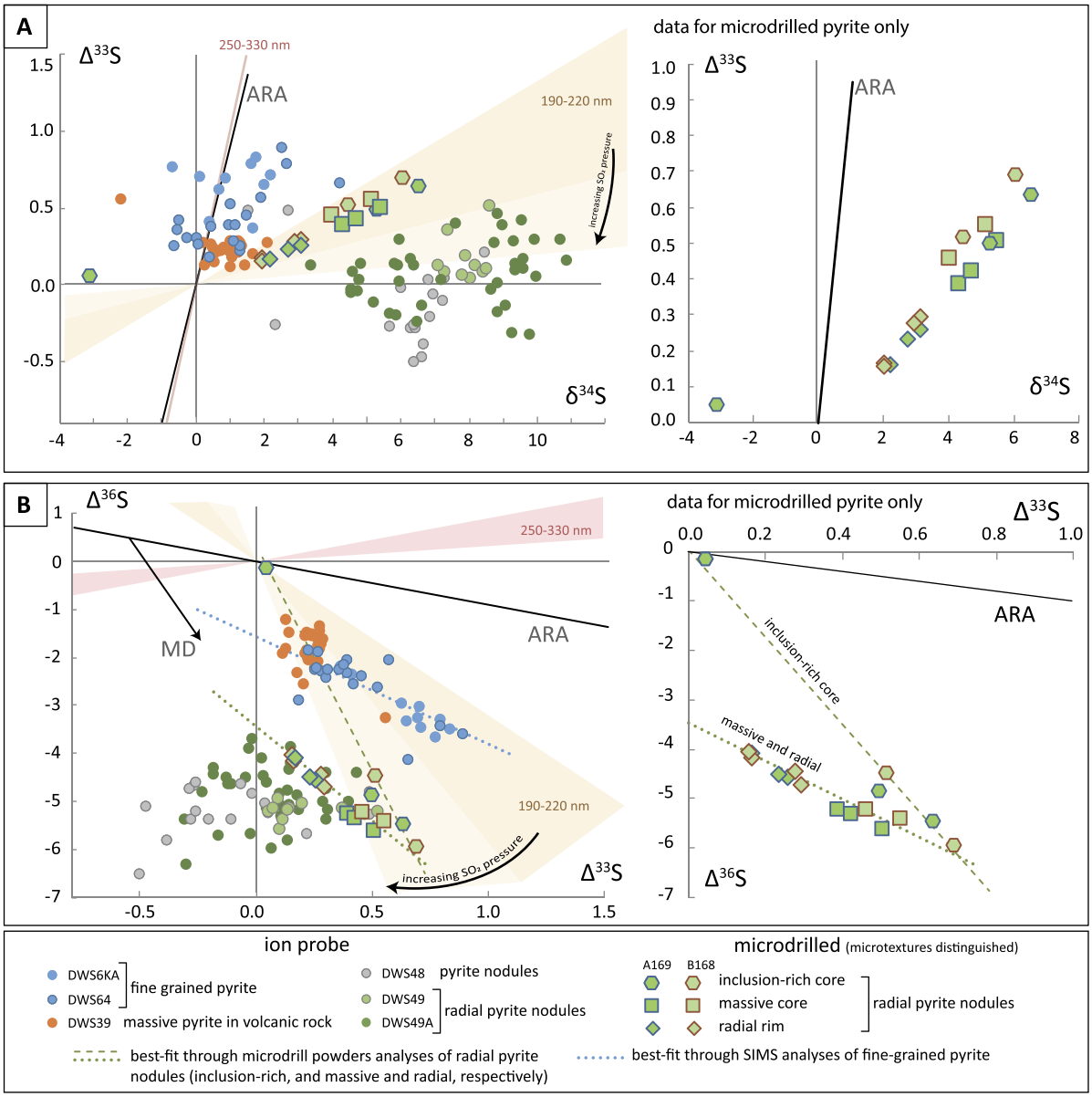

Fig. 4. Quadruple S isotope data for the Dominion Group pyrite. **A** $\Delta^{33}S$ versus $\delta^{34}S$. **B** $\Delta^{36}S$ versus $\Delta^{33}S$. ARA: Archaean reference array, MD: mass-dependent fractionation associated with biologically mediated sulfate reduction (Ono et al., 2006b). S isotope fractionation trends produced by photochemical experiments of photolysis at wavelength of 190-220 nm (Masterson et al., 2011; Ono et al., 2013) and photoexcitation at wavelength of 250-330 nm (Whitehill and Ono, 2012) are shown. Data for microdrilled powders are also plotted separately on the right-hand side of the figure.

pass through the origin and have slopes of around −0.9 to −1.5 (Farquhar et al., 2000; Kaufman et al., 2007).

In situ S isotope analyses

Pyrite nodules (both with radial and non-radial fabrics, samples DWS48, DWS49 and DWS49A) mostly have $\delta^{34}S$ values between +4.5 and +10.8 ‰ and $\Delta^{33}S$ between −0.3 and +0.5 ‰. However, the pyrite nodule without radial texture from sample DWS48 has a slightly larger range of $\delta^{34}S$ values, extending down to +1.5 ‰ ($\delta^{34}S$ < +3 ‰ are from inclusion-rich pyrite cementing euhedral pyrite grains; Fig. 3D and inset), and $\Delta^{33}S$ values down to −0.5 ‰ (Fig. 4B, Supplementary Fig. 2). Values of $\Delta^{36}S$ for the nodules are highly negative, ranging between −6.5 and −3.7 ‰, and resulting in $\Delta^{36}S/\Delta^{33}S$ ratios of −9 or lower. In a core-to-rim traverse, the radially textured pyrite nodule from sample DWS49 has near-constant $\Delta^{33}S$ values in the core (~0.1 ‰) and progressively increasing values in the rim reaching $\Delta^{33}S$ = 0.5 ‰ (Supplementary Fig. 2), while $\delta^{34}S$ values are nearly constant throughout (7.0 to 8.5 ‰). The pyrite nodule from sample DWS49A shows more variable $\Delta^{33}S$ values, without clear core-to-rim trend (Supplementary Fig. 4A).

Fine-grained, semi-massive pyrite from samples DWS6KA and DWS64 has $\delta^{34}S$ values ranging from −0.7 to +4.2 ‰ and $\Delta^{33}S$ values from +0.2 to +0.9 ‰. $\Delta^{36}S$ values of fine-grained, semi-massive pyrite are −4.1 to −1.9 ‰ and in the $\Delta^{36}S$ vs $\Delta^{33}S$ diagram plot along a best-fit line with a slope of −2 that intersects the $\Delta^{36}S$ axis at negative values (Fig. 4B). Volcanic rock sample DWS39 yielded narrow ranges of $\delta^{34}S$ (+0.2–+2.1 ‰) and $\Delta^{33}S$ (+0.1–+0.3 ‰) values. In the $\Delta^{36}S$ vs $\Delta^{33}S$ diagram, the data plot relatively close to the origin.

In summary, the $\Delta^{36}S/\Delta^{33}S$ ratios of −4 and lower of the fine-grained, semi-massive pyrite, pyrite nodules and pyrite hosted in volcanic rocks are markedly different from the ARA.

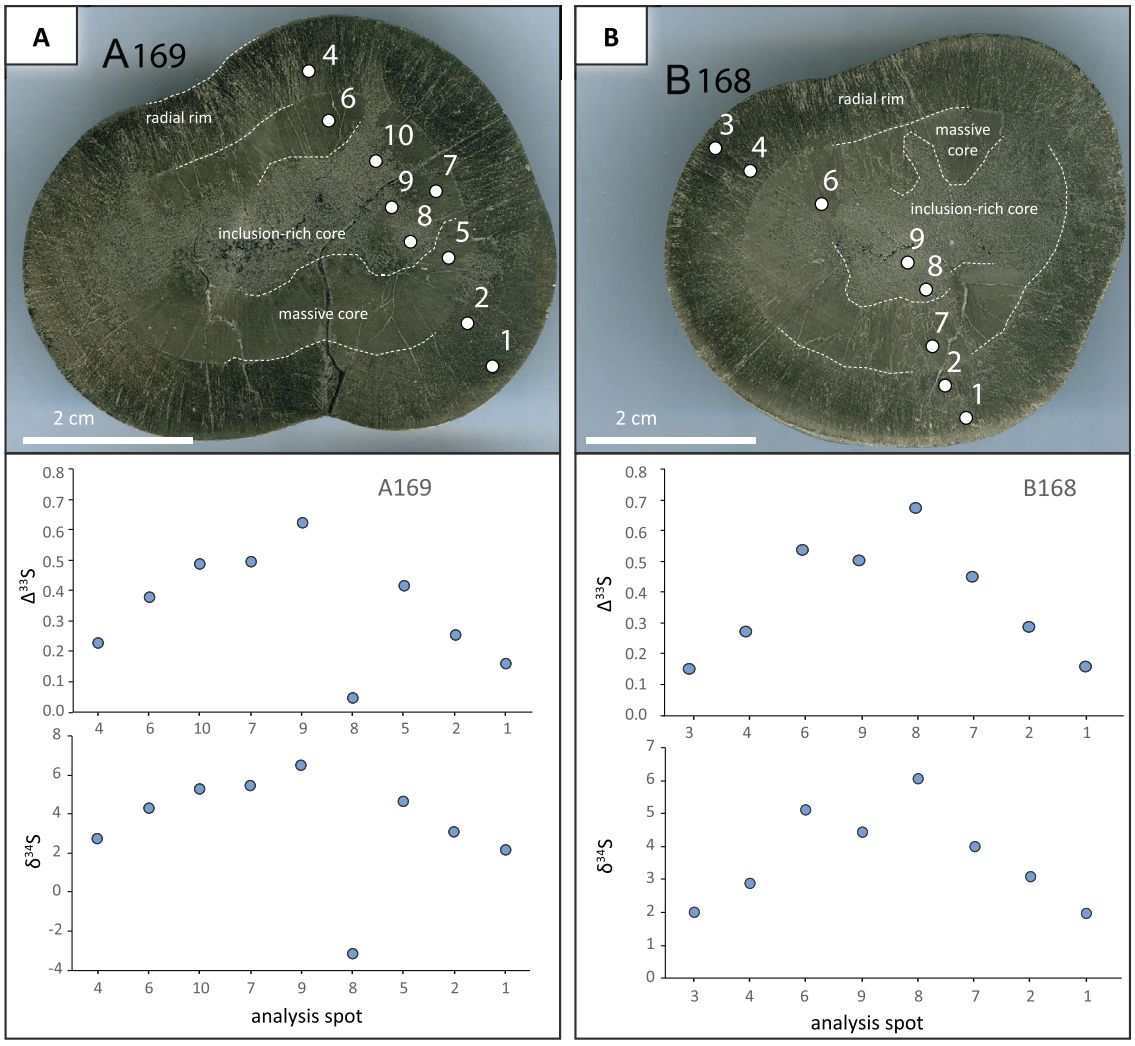

Fig. 5. Textures of pyrite nodules analysed for multiple S-isotope ratios and location of analysis spots. **A** (sample A169) and **B** (sample B168) are radially textured nodules with microdrilled spots shown.

4. Discussion

4.1. Processes responsible for S isotope fractionation trends displayed by the Dominion Group pyrite

The $\delta^{34}S$–$\Delta^{33}S$–$\Delta^{36}S$ systematics of pyrite from the Dominion Group identify two main trends, which are described in detail below.

Shallow $\Delta^{33}S$–$\delta^{34}S$ slope and steep $\Delta^{36}S$–$\Delta^{33}S$ slope: a volcanic photolytic signal of giant volcanic eruption?

The low $\Delta^{33}S/\delta^{34}S$ ratios (mostly < 1), particularly characteristic for radial nodules (Fig. 4A), and the highly negative $\Delta^{36}S/\Delta^{33}S$ ratios (Fig. 4B) are clearly different from the ARA, but are similar to those observed in photolysis experiments of SO_2 using UV light wavelengths of 190–220 nm, whereby SO_2 is photo-dissociated according to the reaction $3SO_2 + h\nu = 2SO_3 + S^0$ (Ono et al., 2013; Whitehill et al., 2015). These experiments produced elemental sulfur (S^0) with markedly positive $\delta^{34}S$ values, low $\Delta^{33}S/\delta^{34}S$ ratios (average 0.09) and steep $\Delta^{36}S/\Delta^{33}S$ slope of −4.6 on average. Product SO_3 and residual SO_2 have negative $\delta^{34}S$ and $\Delta^{33}S$ values, while product S^0 has positive $\delta^{34}S$ and $\Delta^{33}S$ values, as expected from mass balance considerations.

In addition, similar experiments conducted at variable SO_2 gas pressure (Masterson et al., 2011) have demonstrated a strong dependence of $\Delta^{36}S/\Delta^{33}S$ ratios on pressure, with the ratios ranging from approximately −2 at 20 Torr (0.02 bar) to −12 at 800–900 Torr (0.8–0.9 bar). The $\Delta^{36}S/\Delta^{33}S$ ratios of S^0 could also vary significantly depending on atmospheric transparency during photolysis (Masterson et al., 2011). These experimentally generated $\Delta^{36}S/\Delta^{33}S$ ratios are markedly more negative than those typical for sedimentary pyrite from the entire Archaean Eon, ranging from −1 to −1.5 (Farquhar et al., 2007; Kaufman et al., 2007; Thomassot et al., 2015) and only occasionally to as low as −3 (Wacey et al., 2015). This steep $\Delta^{36}S/\Delta^{33}S$ trend passing through the origin is however similar to that observed for some pyrite from Palaeoarchaean barite deposits (Muller et al., 2016; Roerdink et al., 2016). Although the steep array with a slope <-1.5 is rarely observed in Archaean sedimentary rocks, a similar trend has been observed in modern volcanic sulfates preserved in polar ice and snow (Baroni et al., 2007, 2008; Savarino et al., 2003). This trend in MIF-S signature is interpreted to be derived from a SO_2 isotopologue self-shielding effect that is more strongly expressed at high SO_2 partial pressure, a condition that (in the modern, oxygen-rich atmosphere) can only be met during super-large, Plinian eruptions (Lyons, 2009; Whitehill and Ono, 2012) when the volcanic eruption column (plume) reaches into the stratosphere, where low levels of oxygen and ozone allow UV penetration. In the Archaean oxygen-

lacking atmosphere, this trend in MIF-S could have been generated in the troposphere as long as high SO_2 partial pressure has been maintained, which was not the case for most of the Archaean. The combined highly negative $\Delta^{36}S/\Delta^{33}S$ ratios and small $\Delta^{33}S/\delta^{34}S$ values can therefore be considered as a signature of large-volume, subaerial explosive eruptions in the past (Baroni et al., 2007, 2008; Endo et al., 2018; Savarino et al., 2003) and are hereafter referred to as 'volcanic photolytic' trends.

Negative $\Delta^{36}S/\Delta^{33}S$ trends that do not pass through the origin: mixing of S sources

In the $\Delta^{36}S$ versus $\Delta^{33}S$ diagram, some data form apparent linear trends that do not pass through the origin and intersect the $\Delta^{36}S$ axis at negative values (Fig. 4B). Note that, because of mass-balance considerations, one-step photochemical fractionation trends are expected to cross the origin in the $\Delta^{36}S$ versus $\Delta^{33}S$ plot. An offset from the origin with a steeper $\Delta^{36}S/\Delta^{33}S$ slope than that of the ARA has also been observed for Mesoarchaean pyrite of the Witwatersrand Supergroup in South Africa (Guy et al., 2012, 2014; Fig. 6) and Palaeoarchaean pyrite associated with hydrothermal barite in Western Australia and South Africa (Roerdink et al., 2016; Wacey et al., 2015), although the mechanism involved in forming these trends is still unclear. Possible explanations for this shift towards more negative $\Delta^{36}S$ values include: 1) mixing phenomena between mass-independently fractionated sulfur compounds (Fig. 7A); 2) entrainment and mixing of atmospheric, mass-independently fractionated sulfur compounds into an ascending volcanic plume followed by photolytic fractionation of sulfur compounds under high SO_2 gas pressure (Fig. 7B), and 3) mass-dependent microbially induced sulfate reduction (Ono et al., 2006b). These three mechanisms are further discussed below separately.

1 – Mixing of S fractionated along the 'Archaean reference array' ($\Delta^{36}S/\Delta^{33}S \sim -1$) *and 'volcanic photolytic' S recording isotope self-shielding at high SO_2 pressure* ($\Delta^{36}S/\Delta^{33}S \ll -1$). In the $\Delta^{36}S$ versus $\Delta^{33}S$ plot (Fig. 4B), the trends having negative intersection with the $\Delta^{36}S$ axis can be explained by mixing between two S pools, one with positive $\Delta^{33}S$ and negative $\Delta^{36}S$ values (e.g. 'volcanic photolytic' S^0, similar to that produced during 190–220 nm photolysis experiments; Masterson et al., 2011), and another sulfur compound with negative $\Delta^{33}S$ values. For the latter compound, several pathways may be envisaged.

One possible pathway includes fractionation along a trend similar to the 'Archaean reference array' resulting in negative $\Delta^{33}S$ values, $\Delta^{36}S/\Delta^{33}S$ ratios of around -1, and $\delta^{34}S > 0‰$, corresponding to the Palaeoarchaean sedimentary barite record from several cratons (Bao et al., 2007; Roerdink et al., 2012). This sulfate produced in the Archaean anoxic atmosphere may have been reduced via either bacterial (more likely for an organic-rich setting) or thermochemical sulfate reduction.

Another possible mechanism to obtain sulfide with negative $\Delta^{33}S$ values is reduction of SO_3 and residual SO_2 isotopically similar to those produced in experiments of photoexcitation of SO_2 at the wavelength range of 250 nm and higher, which results in $\Delta^{36}S/\Delta^{33}S$ ratios of 0.6 ±0.3 (Whitehill and Ono, 2012; Fig. 4B). Although this signature has rarely been observed in Archaean rocks and is therefore not considered important in Precambrian atmospheric S processes (Ono et al., 2013), its S isotopic systematics matches some S isotope data for pyrite from the Mesoarchaean Witwatersrand Supergroup (da Costa et al., 2020; Guy et al., 2014) and Mozaan Group (Ono et al., 2006a) and could potentially explain our observations (Fig. 6).

A set of mixing trends between 'volcanic photolytic' S derived from S^0 aerosols generated during and following Plinian eruptions and photochemically generated sulfate under 'background' Archean atmospheric conditions is shown by blue arrows in Fig. 7. Variable SO_2 pressure and atmospheric UV transparency expected during a protracted, waxing and waning volcanic eruption could have also contributed to the variations in $\Delta^{33}S/\Delta^{36}S$ ratio observed for different samples and along transects from core to rim in pyrite nodules. The model requires mixing between strongly fractionated end-members to account for the *in situ* data for pyrite nodules that have moderately positive $\delta^{34}S$ and highly negative $\Delta^{33}S$ and $\Delta^{36}S$ values, whereas any data plotting close to these potential end-members are missing (Fig. 4A, B).

2 – Entrainment of atmospheric, mass-independently fractionated sulfur compounds into an ascending volcanic plume followed by mixing with volcanic sulfur and photolytic fractionation of sulfur compounds under high SO_2 gas pressure. In addition to mixing of products of photochemical processes, the two MIF-S-producing processes may have been superimposed and combined via entrainment of atmospheric, mass-independently fractionated S compounds (carrying, for example an ARA signature) into a volcanic plume and mixing with volcanic sulfur gas compounds. Entrainment, warming and expansion of air in a volcanic plume represent the main cause of buoyancy, and allow some volcanic eruption columns to reach 40-50 km altitude (Carey and Bursik, 2015; Sparks, 1986). If photochemically generated atmospheric sulfate with negative $\Delta^{33}S$ and positive $\Delta^{36}S$ and $\delta^{34}S$ values was entrained into a volcanic plume and exchanged with volcanic SO_2 ($\Delta^{33}S = \Delta^{36}S = 0$), 'volcanic photolytic' MIF-S signature would be imparted on already mass-independently fractionated S species, resulting in an initial S isotope composition of sulfur compounds in a volcanic eruption column off the origin in both the $\Delta^{33}S$ vs $\delta^{34}S$ and the $\Delta^{33}S$ vs $\Delta^{36}S$ plots. The extent of this shift would depend on the amount of entrained atmospheric S relative to the volcanic S in the volcanic eruption column. Entrainment and mixing of atmospheric and volcanic S species in various proportions would result in an array of volcanic fractionation lines, which could explain almost the full distribution of our analyses, in particular the in situ analyses of nodular pyrite in the $\Delta^{33}S$ vs $\Delta^{36}S$ plot (Fig. 4, 5B).

3 – Mass-dependent sulfate reduction. Microbially induced sulfate reduction can produce mass-dependent S isotope fractionation with $\delta^{33}S/\delta^{34}S$ ratios that slightly deviate from the 0.515 reference line (Johnston et al., 2008a). Analyses of Phanerozoic pyrite have revealed that these microbial processes can produce $\Delta^{36}S$ values as low as −2.4 ‰ in association with $\delta^{34}S$ values down to −23 ‰, and an average $\Delta^{36}S/\Delta^{33}S$ slope of around −6.8 (Johnston et al., 2008a, 2008b; Ono et al., 2006b; MD arrow in Fig. 4B). Using this $\Delta^{36}S/\Delta^{33}S$ slope, reduction of photochemically produced sulfate with S isotope values corresponding to the ARA could potentially account for the deviation observed. However, to match our results this mechanism would require a shift in $\Delta^{36}S$ values of up to 7 ‰, well beyond the range of $\Delta^{36}S$ values of 2.4 ‰ that has been measured in Phanerozoic pyrite (Ono et al., 2006b). In addition, the large range of $\delta^{34}S$ values that should have accompanied this process was not observed in our study. Thus, mass-dependent sulfate reduction is not considered to be the relevant process to explain very low $\Delta^{36}S$ values observed in this study.

Quadruple sulfur isotope data do not allow to resolve between the models 1 and 2. Both models result in temporal and spatial heterogeneities in the $\Delta^{36}S/\Delta^{33}S$ ratio with time and distance from the eruption centre as the volcanic plume ascended, entrained ambient atmosphere, spreads away from the eruption centre, and SO_2 gas pressure in the plume progressively decreased (resulting in smaller $\Delta^{36}S/\Delta^{33}S$ ratio). Both mixing models explain the majority of our data, but mass-dependent fractionation mechanisms might have also been involved as indicated by data plotting

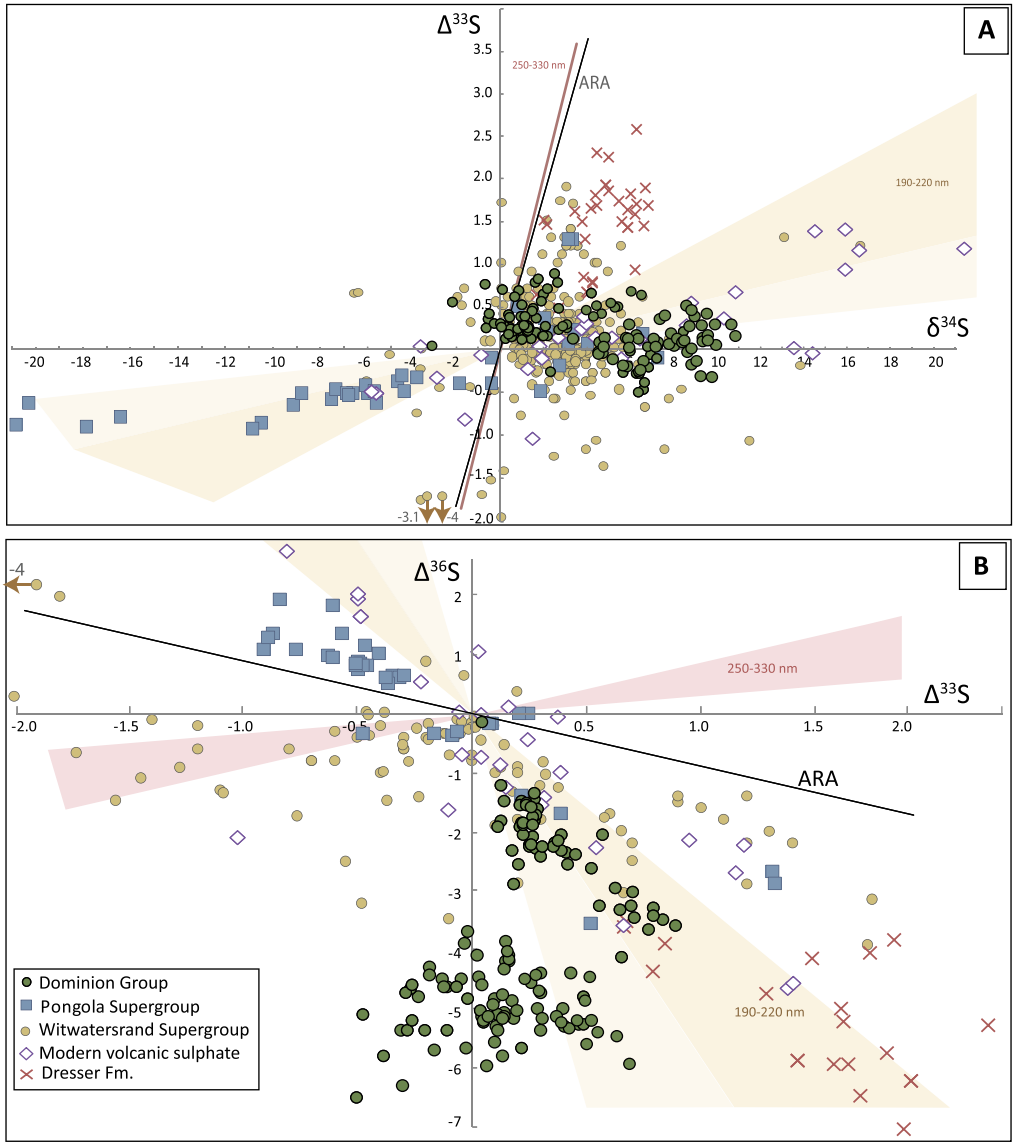

Fig. 6. S isotope composition (**A** $\Delta^{33}S$ versus $\delta^{34}S$, **B** $\Delta^{36}S$ versus $\Delta^{33}S$) of pyrite from the Dominion Group compared with pyrite from the Witwatersrand Supergroup (Guy et al., 2014), Pongola Supergroup (Ono et al., 2006a; Eickmann et al., 2018), Dresser Formation (Wacey et al., 2015) and modern, photochemically generated, atmospheric sulfate aerosols that are produced during very large volcanic eruptions when a volcanic eruption plume reaches the atmosphere (Baroni et al., 2007, 2008; Savarino et al., 2003).

in Fig. 4A into the quadrant with negative $\delta^{34}S$ and positive $\Delta^{33}S$ values. Considering the high organic carbon content of the sediments in which pyrite formed and the lacustrine setting, microbial sulfate reduction of S compounds delivered from the atmosphere to the lake seems likely. However, due to a low sulfate content in this lacustrine setting and in general in Archaean surface environments, quantitative sulfate reduction within sediments and water column left no obvious signature of microbial sulfate reduction in S isotope systematics. Regardless of the mixing pathway involved, the Dominion Group pyrite nodules record volcanic photolysis and mixing with a 'background' Archean atmospheric signal. We suggest below that this signal had a better potential to be preserved and retain its unique characteristics in terrestrial settings with high sedimentation rates.

4.2. Effect of contrasting depositional timescales on continental vs marine S records

The quadruple-S isotope systematics of the Dominion Group pyrite is strikingly different from the ARA and has a strong similarity with that of modern volcanic sulfate aerosols formed in the stratosphere (where low oxygen and ozone contents allowed UV penetration) and preserved in Antarctic ice and ash layers (Baroni et al., 2008; Savarino et al., 2003). This is possibly due to deposition of S aerosols in lakes during the Dominion Group volcanism and stratospheric volcanic sulfate in snow in modern times, which in both cases allowed preservation of transient atmospheric signals, representing 'snapshots' of relatively short-lived, MIF-S-generating events. Importantly, in the case of the Archaean oxygen- and ozone-free atmosphere, similar photochemical reactions were not confined to the stratosphere, and could have occurred at any altitude through the atmosphere. In contrast, the Archaean marine realms would allow to sustain, recycle and homogenise S inputs impacted by various photochemical and aqueous reactions with correspondingly different MIF-S and MDF-S signals (Endo et al., 2016; Halevy, 2013).

As photolysis-derived sulfate and elemental sulfur aerosols were deposited in Archaean oceans, their S isotope composition was modified in a larger S-pool over a longer time compared to lacustrine systems and local or short-term isotopic perturba-

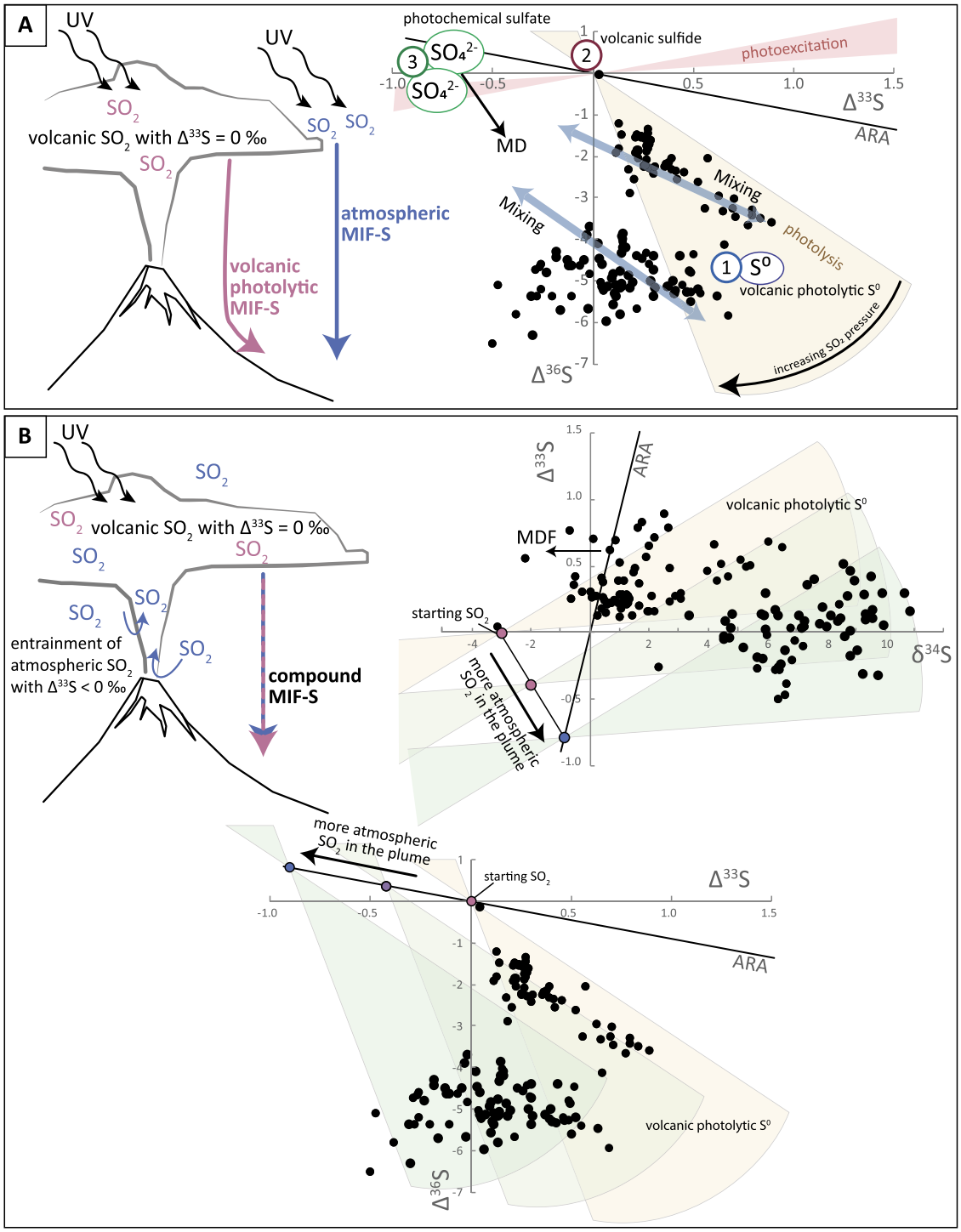

Fig. 7. Two models of MIF-S production and possible S sources. **A** Production of MIF-S in the atmosphere ('background' S species with ARA compositions) and in a volcanic plume with high SO_2 gas pressure ('volcanic photolytic' MIF-S). MIF-S pools produced via these two processes mix upon deposition. 1 – Atmospheric S of photochemical origin produced during super-large volcanic eruptions as defined by 190-220 nm UV photolysis experiments (Masterson et al., 2011; Ono et al., 2013); 2 – Mass-dependent sulfur derived from volcanic source and not processed in the atmosphere; 3 – Photochemically generated MIF-S in sulfate with $\Delta^{33}S < 0$ ‰, matching in S isotope composition either the ARA ($\Delta^{36}S/\Delta^{33}S \sim 0.9$) or products of photochemical experiments at 250-330 nm wavelength ($\Delta^{36}S/\Delta^{33}S \sim 0.6$). Arrows show possible mixing trends. Changing SO_2 pressure in a waxing and waning volcanic plume would result in variations in the $\Delta^{36}S/\Delta^{33}S$ slope. **B** Entrainment of Archaean 'background' atmospheric S species into a volcanic eruption plume and production of 'volcanic photolytic' MIF-S starting with a mixture of volcanic S species with $\Delta^{36}S = \Delta^{33}S = 0$ ‰ and 'background' atmospheric S carrying ARA MIF-S. Increasing proportion of atmospheric S entrained into the volcanic plume will result in a progressive shift of the starting composition for 'volcanic photolytic' MIF-S away from the origin in both $\Delta^{36}S$ vs $\Delta^{33}S$ and $\Delta^{33}S$ vs $\delta^{34}S$ plots.

tions were not immediately transferred to the rock record (Halevy, 2013). In contrast, sediments deposited in small and short-lived intracratonic basins with high sedimentation rate had higher potential to preserve transient MIF-S signals.

The nature of atmospheric S species deposited on land in the Archaean is unclear. Studies of multiple S isotope composition of pyrite from Archaean terrestrial deposits, including palaeosols, diamictites, fluvial deposits and conglomerates have found relatively

small ranges in $\Delta^{33}S$ values with a prevalence of near-zero to slightly negative values (Guy et al., 2012, 2014; Hofmann et al., 2009; Maynard et al., 2013). These results may reflect the interaction between exposed surface of landmasses and highly reactive, sulfuric acid in groundwater, rivers and continental run-off derived from atmospheric sulfate aerosols with negative $\Delta^{33}S$ values. Conversely and complementarily, the less reactive and soluble elemental S with positive $\Delta^{33}S$ values may have been preferentially transported off landmasses as a part of the sedimentary load and eventually deposited with marine shales (Maynard et al., 2013).

5. Conclusions

Quadruple S isotope data for pyrite from lacustrine sedimentary rocks of the Dominion Group in South Africa indicate mixing of S pools, shedding light on the S-cycle of a Mesoarchaean volcanic lake. Overall, the data provide evidence for two independent photolytic trends: 1) a trend similar to the 'Archaean reference array', which is pervasively preserved in marine sedimentary rocks spanning the entire Archaean and represents an Archaean 'background' signal, and 2) a 'volcanic photolytic' trend, with a steeper slope in $\Delta^{33}S$ vs $\Delta^{36}S$ space, which appears to be recording a discrete, super-large volcanic eruption event.

The strongly ^{36}S-depleted S isotope composition implies the operation of specific photochemical reactions that resulted in S isotope systematics different from the more commonly observed $\Delta^{36}S$–$\Delta^{33}S$ trends (e.g., ARA). The $\Delta^{36}S/\Delta^{33}S$ ratios of −4 and lower ('volcanic photolytic' trend) resemble the composition of sulfate aerosols produced during exceptionally large modern stratospheric eruptions, and are consistent with their production in a dense, optically thick SO_2-rich volcanic plume at any altitude in the Archaean, oxygen-deficient atmosphere. This interpretation is also consistent with the geological context of the succession. By extension, the absence of such trend in the Archaean 'background' records provides a constraint for the maximum atmospheric SO_2 level in the Archaean.

Another implication of our study is that some variations in the $\Delta^{36}S/\Delta^{33}S$ ratios could be generated through mixing of 'volcanic photolytic' S with S affected by Archaean 'background' photochemical processes or entrainment of Archean 'background' atmospheric, mass-independently fractionated sulfur compounds into an ascending volcanic plume followed by mixing with volcanic sulfur and photolytic fractionation of sulfur compounds under high SO_2 gas pressure. Our study thus suggests that some variations in $\Delta^{36}S/\Delta^{33}S$ ratio in the Archean sedimentary records might reflect waxing and waning of subaerial volcanism rather than, and not necessarily through, whole-scale changes in atmospheric composition.

CRediT authorship contribution statement

Andrea Agangi: writing, conceptualization, **Axel Hofmann:** conceptualization, editing, **Benjamin Eickmann:** data curation, editing, **Frantz Ossa Ossa:** data curation, editing, **Perinne Tyler:** data curation, editing, **Boswell Wing:** data curation, editing, and **Andrey Bekker:** supervision, editing.

Declaration of competing interest

The authors declare that they have no known competing financial interests or personal relationships that could have appeared to influence the work reported in this paper.

Acknowledgement

This paper has benefitted from the comments of associated editor F. Moynier and two anonymous reviewers, which are greatly appreciated. Economic support from CIMERA (Centre of Excellence for Mineral and Energy Resources) hosted at the University of Johannesburg has been instrumental at various stages of this study. Participation by AB was supported by the Discovery and Accelerator Grants from the Natural Sciences and Engineering Research Council of Canada (NSERC) and the Petroleum Fund of the American Chemical Society. BAW acknowledges NSF-EF1724393.

Appendix A. Supplementary material

Supplementary material related to this article can be found online at https://doi.org/10.1016/j.epsl.2022.117737.

References

Agangi, A., Hofmann, A., Hegner, E., Xie, H., Teschner, C., Slabunov, A., Svetov, S.A., 2020. The Mesoarchaean Dominion Group and the onset of intracontinental volcanism on the Kaapvaal craton – geological, geochemical and temporal constraints. Gondwana Res. 84, 131–150.

Agangi, A., Hofmann, A., Ossa Ossa, F., Paprika, D., Bekker, A., 2021. Mesoarchaean acidic volcanic lakes: a critical ecological niche in early land colonisation. Earth Planet. Sci. Lett. 556, 116725.

Armstrong, R.A., Compston, W., Retief, E.A., Williams, I.S., Welke, H.J., 1991. Zircon ion microprobe studies bearing on the age and evolution of the Witwatersrand triad. Precambrian Res. 53, 243–266.

Bao, H., Rumble III, D., Lowe, D.R., 2007. The five stable isotope compositions of Fig Tree barites: implications on sulfur cycle in ca. 3.2-Ga oceans. Geochim. Cosmochim. Acta 71, 4868–4879.

Baroni, M., Savarino, J., Cole-Dai, J., Rai, V.K., Thiemens, M.H., 2008. Anomalous sulfur isotope compositions of volcanic sulfate over the last millennium in Antarctic ice cores. J. Geophys. Res., Atmos. 113.

Baroni, M., Thiemens, M.H., Delmas, R.J., Savarino, J., 2007. Mass-independent sulfur isotopic compositions in stratospheric volcanic eruptions. Science 315, 84–87.

Bekker, A., Barley, M.E., Fiorentini, M.L., Rouxel, O.J., Rumble, D., Beresford, S.W., 2009. Atmospheric sulfur in archean komatiite-hosted nickel deposits. Science 326, 1086–1089.

Canfield, D.E., 2005. The early history of atmospheric oxygen: homage to Robert M. Garrels. Annu. Rev. Earth Planet. Sci. 33, 1–36.

Canfield, D.E., Habicht, K.S., Thamdrup, B., 2000. The Archean sulfur cycle and the early history of atmospheric oxygen. Science 288, 658–661.

Carey, S., Bursik, M., 2015. Chapter 32 - Volcanic plumes. In: Sigurdsson, H. (Ed.), The Encyclopedia of Volcanoes, second edition. Academic Press, Amsterdam, pp. 571–585.

Catling, D.C., Zahnle, K.J., 2020. The Archean atmosphere. Sci. Adv. 2020 (6), eaax1420. https://doi.org/10.1126/sciadv.aax1420.

Crowe, S.A., Paris, G., Katsev, S., Jones, C., Kim, S.-T., Zerkle, A.L., Nomosatryo, S., Fowle, D.A., Adkins, J.F., Sessions, A.L., Farquhar, J., Canfield, D.E., 2014. Sulfate was a trace constituent of Archean seawater. Science 346, 735–739.

da Costa, G., Hofmann, A., Agangi, A., 2020. A revised classification scheme of pyrite in the Witwatersrand Basin and application to placer gold deposits. Earth-Sci. Rev. 201.

Eickmann, B., Hofmann, A., Wille, M., Bui, T.H., Wing, B.A., Schoenberg, R., 2018. Isotopic evidence for oxygenated Mesoarchaean shallow oceans. Nat. Geosci. 11, 133–138.

Endo, Y., Danielache, S.O., Ueno, Y., 2018. Total pressure dependence of sulfur mass-independent fractionation by SO2 photolysis. Geophys. Res. Lett. 46, 483–491.

Endo, Y., Ueno, Y., Aoyama, S., Danielache, S.O., 2016. Sulfur isotope fractionation by broadband UV radiation to optically thin SO2 under reducing atmosphere. Earth Planet. Sci. Lett. 453, 9–22.

Farquhar, J., Bao, H., Thiemens, M., 2000. Atmospheric influence of Earth's earliest sulfur cycle. Science 289, 756–758.

Farquhar, J., Peters, M., Johnston, D.T., Strauss, H., Masterson, A., Wiechert, U., Kaufman, A.J., 2007. Isotopic evidence for Mesoarchaean anoxia and changing atmospheric sulphur chemistry. Nature 449, 706–709.

Farquhar, J., Savarino, J., Airieau, S., Thiemens, M., 2001. Observation of wavelength-sensitive mass-independent sulfur isotope ejects during SO2 photolysis: implications for the early atmosphere. J. Geophys. Res., Solid Earth 106, 32829–32839.

Grandstaff, D.E., Edelman, M.J., Foster, R.W., Zbinden, E., Kimberley, M.M., 1986. Chemistry and mineralogy of Precambrian paleosols at the base of the Dominion and Pongola Groups (Transvaal, South Africa). Precambrian Res. 32, 97–131.

Guy, B.M., Ono, S., Gutzmer, J., Kaufman, A.J., Lin, Y., Fogel, M.L., Beukes, N.J., 2012. A multiple sulfur and organic carbon isotope record from non-conglomeratic sedimentary rocks of the Mesoarchean Witwatersrand Supergroup, South Africa. Precambrian Res. 216–219, 208–231.

Guy, B.M., Ono, S., Gutzmer, J., Lin, Y., Beukes, N.J., 2014. Sulfur sources of sedimentary "buckshot" pyrite in the auriferous conglomerates of the Mesoarchean Witwatersrand and Ventersdorp Supergroups, Kaapvaal Craton, South Africa. Miner. Depos. 49, 751–775.

Habicht, K.S., Gade, M., Thamdrup, B., Berg, P., Canfield, D.E., 2002. Calibration of sulfate levels in the Archean ocean. Science 298, 2372–2374.
Halevy, I., 2013. Production, preservation, and biological processing of mass-independent sulfur isotope fractionation in the Archean surface environment. Proc. Natl. Acad. Sci. 110, 17644–17649.
Hofmann, A., Bekker, A., Rouxel, O., Rumble, D., Master, S., 2009. Multiple sulphur and iron isotope composition of detrital pyrite in Archaean sedimentary rocks: a new tool for provenance analysis. Earth Planet. Sci. Lett. 286, 436–445.
Jackson, M.C., 1992. A review of the Late Archaean volcano-sedimentary Dominion Group and implications for the tectonic setting of the Witwatersrand Supergroup, South Africa. J. Afr. Earth Sci. 15, 169–186.
Johnston, D.T., Farquhar, J., Habicht, K.S., Canfield, D.E., 2008a. Sulphur isotopes and the search for life: strategies for identifying sulphur metabolisms in the rock record and beyond. Geobiology 6, 425–435.
Johnston, D.T., Farquhar, J., Summons, R.E., Shen, Y., Kaufman, A.J., Masterson, A.L., Canfield, D.E., 2008b. Sulfur isotope biogeochemistry of the Proterozoic McArthur Basin. Geochim. Cosmochim. Acta 72, 4278–4290.
Kaufman, A.J., Johnston, D.T., Farquhar, J., Masterson, A.L., Lyons, T.W., Bates, S., Anbar, A.D., Arnold, G.L., Garvin, J., Buick, R., 2007. Late Archean biospheric oxygenation and atmospheric evolution. Science 317, 1900–1903.
Lyons, J.R., 2009. Atmospherically-derived mass-independent sulfur isotope signatures, and incorporation into sediments. Chem. Geol. 267, 164–174.
Masterson, A.L., Farquhar, J., Wing, B.A., 2011. Sulfur mass-independent fractionation patterns in the broadband UV photolysis of sulfur dioxide: pressure and third body effects. Earth Planet. Sci. Lett. 306, 253–260.
Maynard, J.B., Sutton, S.J., Rumble Iii, D., Bekker, A., 2013. Mass-independently fractionated sulfur in Archean paleosols: a large reservoir of negative $\Delta 33S$ anomaly on the early Earth. Chem. Geol. 362, 74–81.
Muller, É., Philippot, P., Rollion-Bard, C., Cartigny, P., 2016. Multiple sulfur-isotope signatures in Archean sulfates and their implications for the chemistry and dynamics of the early atmosphere. Proc. Natl. Acad. Sci. 113, 7432–7437.
Nel, L.T., Jacobs, H., Allan, J.T., Bozzoli, G.R., 1937. Wonderstone. Geol. Surv. South Afr. Bull. 8.
Ohmoto, H., Watanabe, Y., Ikemi, H., Poulson, S.R., Taylor, B.E., 2006. Sulphur isotope evidence for an oxic Archaean atmosphere. Nature 442 (7105), 908–911.
Ono, S., Beukes, N.J., Rumble, D., Fogel, M.L., 2006a. Early evolution of atmospheric oxygen from multiple-sulfur and carbon isotope records of the 2.9 Ga Mozaan Group of the Pongola Supergroup, Southern Africa. S. Afr. J. Geol. 109, 97–108.
Ono, S., Whitehill, A.R., Lyons, J.R., 2013. Contribution of isotopologue self-shielding to sulfur mass-independent fractionation during sulfur dioxide photolysis. J. Geophys. Res., Atmos. 118, 2444–2454.
Ono, S., Wing, B., Johnston, D., Farquhar, J., Rumble, D., 2006b. Mass-dependent fractionation of quadruple stable sulfur isotope system as a new tracer of sulfur biogeochemical cycles. Geochim. Cosmochim. Acta 70, 2238–2252.
Paprika, D., Hofmann, A., Agangi, A., Elburg, M., Xie, H., Hartmann, S., 2021. Age of the Dominion-Nsuze Igneous Province, the first intracratonic Igneous Province of the Kaapvaal Craton. Precambrian Res. 363, 106335.
Pavlov, A.A., Kasting, J.F., 2002. Mass-independent fractionation of sulfur isotopes in Archean sediments: strong evidence for an anoxic Archean atmosphere. Astrobiology 2, 27–41.
Robb, L.J., Meyer, F.M., 1995. The Witwatersrand Basin, South Africa: geological framework and mineralization processes. Ore Geol. Rev. 10, 67–94.
Roerdink, D.L., Mason, P.R.D., Farquhar, J., Reimer, T., 2012. Multiple sulfur isotopes in Paleoarchean barites identify an important role for microbial sulfate reduction in the early marine environment. Earth Planet. Sci. Lett. 331–332, 177–186.
Roerdink, D.L., Mason, P.R.D., Whitehouse, M.J., Brouwer, F.M., 2016. Reworking of atmospheric sulfur in a Paleoarchean hydrothermal system at Londozi, Barberton Greenstone Belt, Swaziland. Precambrian Res. 280, 195–204.
Savarino, J., Romero, A., Cole-Dai, J., Bekki, S., Thiemens, M.H., 2003. UV induced mass-independent sulfur isotope fractionation in stratospheric volcanic sulfate. Geophys. Res. Lett. 30, 2131.
Sparks, R.S.J., 1986. The dimensions and dynamics of volcanic eruption columns. Bull. Volcanol. 48, 3–15.
Thomassot, E., O'Neil, J., Francis, D., Cartigny, P., Wing, B.A., 2015. Atmospheric record in the Hadean Eon from multiple sulfur isotope measurements in Nuvvuagittuq Greenstone Belt (Nunavik, Quebec). Proc. Natl. Acad. Sci. 112, 707–712.
Ueno, Y., 2014. Coping with low ocean sulfate. Science 346, 703–704.
Von Backström, J.W., 1962. Die geologie van die gebied om Ottosdal, Transvaal, Toeligting van blaaie 2625D (Barberspan) en 2626C (Ottosdal). Die Staatsdrukker.
Wacey, D., Noffke, N., Cliff, J., Barley, M.E., Farquhar, J., 2015. Micro-scale quadruple sulfur isotope analysis of pyrite from the ~3480 Ma Dresser Formation: new insights into sulfur cycling on the early Earth. Precambrian Res. 258, 24–35.
Whitehill, A.R., Jiang, B., Guo, H., Ono, S., 2015. SO2 photolysis as a source for sulfur mass-independent isotope signatures in stratospehric aerosols. Atmos. Chem. Phys. 15, 1843–1864.
Whitehill, A.R., Ono, S., 2012. Excitation band dependence of sulfur isotope mass-independent fractionation during photochemistry of sulfur dioxide using broadband light sources. Geochim. Cosmochim. Acta 94, 238–253.
Zerkle, A.L., Claire, M.W., Domagal-Goldman, S.D., Farquhar, J., Poulton, S.W., 2012. A bistable organic-rich atmosphere on the Neoarchaean Earth. Nat. Geosci. 5, 359–363.